Loughborough University

This item was submitted to Loughborough's Research Repository by the author.
Items in Figshare are protected by copyright, with all rights reserved, unless otherwise indicated.

Reconstruction of landslide movements by inversion of 4D electrical resistivity tomography monitoring data

PLEASE CITE THE PUBLISHED VERSION

http://dx.doi.org/10.1002/2015GL067494

PUBLISHER

American Geophysical Union (AGU) ; Wiley © The Authors

VERSION

VoR (Version of Record)

PUBLISHER STATEMENT

This work is made available according to the conditions of the Creative Commons Attribution 4.0 International (CC BY 4.0) licence. Full details of this licence are available at: http://creativecommons.org/licenses/ by/4.0/

LICENCE

CC BY 4.0

REPOSITORY RECORD

Wilkinson, Paul, J. Chambers, S. Uhlemann, Philip Meldrum, Alister Smith, Neil Dixon, and Meng H. Loke. 2016. “Reconstruction of Landslide Movements by Inversion of 4D Electrical Resistivity Tomography Monitoring Data”. Loughborough University. https://hdl.handle.net/2134/20448.

AGU PUBLICATIONS

Geophysical Research Letters

RESEARCH LETTER
10.1002/2015GL067494

Key Points:
- ERT monitoring of landslides requires knowledge of electrode movements that can be costly to obtain
- An inverse method can be used to reconstruct electrode movements from geoelectrical monitoring data
- First field demonstration of ERT time-lapse movement inversion over timescales of days to years

Supporting Information:
- Text S1, Figures S1 and S2, and Tables S1–S5
- Figure S1
- Figure S2

Correspondence to:
P. Wilkinson,
pbw@bgs.ac.uk

Citation:
Wilkinson, P., J. Chambers, S. Uhlemann, P. Meldrum, A. Smith, N. Dixon, and M. H. Loke (2016), Reconstruction of landslide movements by inversion of 4-D electrical resistivity tomography monitoring data, *Geophys. Res. Lett.*, *43*, doi:10.1002/2015GL067494.

Received 17 DEC 2015
Accepted 19 JAN 2016
Accepted article online 22 JAN 2016

©2016. The Authors.
This is an open access article under the terms of the Creative Commons Attribution License, which permits use, distribution and reproduction in any medium, provided the original work is properly cited.

Reconstruction of landslide movements by inversion of 4-D electrical resistivity tomography monitoring data

Paul Wilkinson[1], Jonathan Chambers[1], Sebastian Uhlemann[1,2], Philip Meldrum[1], Alister Smith[3], Neil Dixon[3], and Meng Heng Loke[4]

[1]Environmental Science Centre, British Geological Survey, Nottingham, UK, [2]Institute of Geophysics, ETH Zürich, Zürich, Switzerland, [3]School of Civil and Building Engineering, Loughborough University, Loughborough, UK, [4]Geotomo Software, Gelugor, Malaysia

Abstract Reliable tomographic inversion of geoelectrical monitoring data from unstable slopes relies critically on knowing the electrode positions, which may move over time. We develop and present an innovative inverse method to recover movements in both surface directions from geoelectrical measurements made on a grid of monitoring electrodes. For the first time, we demonstrate this method using field data from an active landslide to recover sequences of movement over timescales of days to years. Comparison with GPS measurements demonstrated an accuracy of within 10% of the electrode spacing, sufficient to correct the majority of artifacts that would occur in subsequent image reconstructions if incorrect positions are used. Over short timescales where the corresponding subsurface resistivity changes were smaller, the constraints could be relaxed and an order-of-magnitude better accuracy was achievable. This enabled the onset and acceleration of landslide activity to be detected with a temporal resolution of a few days.

1. Introduction

Landslides, whether occurring on natural or engineered slopes, can pose significant health and economic risks to communities and infrastructure. Prolonged and severe rainfall events are known to cause the majority of shallow landslides by reducing the internal soil strength and increasing the downslope forces [*Lehmann and Or*, 2012; *Bogaard and Greco*, 2015]. Much effort is therefore being applied to understanding hydraulic triggering mechanisms for slope failure, especially in the presence of ongoing climate change [*Dijkstra et al.*, 2014]. There is increasing interest in using time-lapse electrical resistivity tomography (ERT) monitoring to investigate such problems [*Perrone et al.*, 2014] due to the strong dependence of resistivity on moisture content, the volumetric nature of the images generated, and the relatively high temporal and spatial resolutions that can be achieved compared to intrusive methods [*Sjodahl et al.*, 2009, 2010; *Niesner*, 2010; *Lebourg et al.*, 2010; *Wilkinson et al.*, 2010; *Bièvre et al.*, 2012; *Supper et al.*, 2014; *Chambers et al.*, 2014; *Gunn et al.*, 2014].

The British Geological Survey (BGS), in collaboration with international partner organizations, has developed a landslide observatory where various monitoring methods are being applied to an active slow moving landslide. The core technique, which has been active since 2008, is 4-D ERT [*Wilkinson et al.*, 2010; *Chambers et al.*, 2011]. This has been supplemented over the years by manually or remotely controlled sensors and techniques including a weather station, temperature sensors, and soil moisture probes [*Gunn et al.*, 2013]; GPS monitoring of ground surface marker pegs [*Uhlemann et al.*, 2015a]; shape accelerometer arrays (SAAs), inclinometers, tilt meters, active acoustic waveguides, and piezometers [*Smith et al.*, 2014; *Dixon et al.*, 2015].

Although changes in ERT monitoring images can reveal information about hydraulic processes, care must be taken when applying the technique to unstable slopes because geoelectrical measurements depend critically on the positions of the electrodes. If, due to ground movement, the positions are no longer accurately known, the tomographic images can be seriously distorted often obscuring changes due to moisture content variations [*Zhou and Dahlin*, 2003; *Oldenborger et al.*, 2005; *Wilkinson et al.*, 2008, 2010, 2015; *Uhlemann et al.*, 2015a]. It would be impractical and expensive to survey the positions of the electrodes with a suitable accuracy and frequency to match the ERT data acquisition schedule. Besides which, electrodes are often buried and not visible from the surface. But recent research has shown that electrode position information can be obtained from time-lapse ERT data using inverse methods, many of which are still in development [*Wilkinson et al.*, 2010; *Giannakis et al.*, 2012; *Boyle et al.*, 2014; *Kim et al.*, 2014; *Loke et al.*, 2015]. Here we present the first field demonstration to show that an inverse method can be used to track surface displacements

of electrodes on an unstable slope using only 4-D ERT data. By modifying and applying inversion methods previously applied to time-lapse 2-D field data and 3-D laboratory data [*Wilkinson et al*., 2010, 2015] we show that quantitative information on the magnitude, direction, and timing of electrode movements can be recovered from 4-D ERT field data over timescales ranging from days to years, effectively turning ERT imaging arrays into motion-sensing grids. Rather than considering the effects of moving electrodes to be unavoidable data artifacts, this innovative approach makes greater use of the information content of the time-lapse geoelectrical data, allowing surface deformations to be monitored at the same spatial and temporal scales as the causative changes in the internal hydrogeophysical state. It complements other recently developed geophysical inverse methods for monitoring and understanding dynamic landslide processes, such as broadband or multiperiod seismic inversion [*Yamada et al*., 2013; *Hibert et al*., 2014] and surface displacement inversion [*Aryal et al*., 2015; *Booth et al*., 2013].

2. Field Site and Data

The Hollin Hill landslide observatory is set on a slow to very slow moving multiple earth slide-earth flow located near the town of Malton, UK (Figure 1). The site is a south facing hill with a mean slope angle of 14°. The bedrock geology comprises four formations of Lower and Middle Jurassic age. From the base to the top of the slope, these are the Lias Group Redcar Mudstone Formation (RMF), Staithes Sandstone and Cleveland Ironstone Formation (SSF), and Whitby Mudstone Formation (WMF), which are overlain at the top of the hill by the Dogger Formation (DF). The bedrock exhibits a gentle dip of a few degrees to the north [*Chambers et al*., 2011]. The WMF is the failing formation at the site, and both the WMF and SSF are highly weathered with low stiffnesses of 1–5 MPa [*Gunn et al*., 2013]. Figure 1 shows the geomorphology of the site. At the top of the slope, within the WMF, the site is dominated by the main scarp of the landslide which exhibits rotational failure surfaces. Further toward the base, earth flows have developed where the WMF has moved over the SSF, forming several lobes. Borehole logs from the western lobe indicate a maximum thickness of landslide deposits of approximately 5 m. More detailed geomorphological characterizations are presented in *Merritt et al*. [2014] and *Uhlemann et al*. [2015b].

The landslide is permanently instrumented with many types of sensors, including an ERT electrode array (shown by red and green colored circles in Figure 1), weather station (light blue chevron), and SAA (yellow triangle). The SAA is a borehole sensor, containing a string of micro electromechanical accelerometers [*Abdoun et al*., 2012], that logs borehole deformations over a range of depths at hourly intervals. The ERT array is a grid of 5×32 permanently installed stainless steel electrodes. The spacing of electrodes in the y direction (along the lines) is ~4.75 m, and the interline spacing (in the x direction) is ~9.5 m. The array is connected to a BGS-designed automated geoelectrical monitoring system [*Wilkinson et al*., 2010], which has performed a sequence of measurements on alternating days from March 2008 onward (subject to occasional interruptions due to system, battery, or communication problems). On each of the five lines, these consisted of inline dipole-dipole measurements with dipole lengths a of 4.75–19 m and dipole separations na, where $n = 1$–8. Each measurement was made in reciprocal configurations, with the mean of the reciprocal data being taken as the measured value and the standard error in the mean (referred to as the reciprocal error) being used as a measure of data quality [*LaBrecque et al*., 1996]. Data were filtered out on the basis of (i) having negative apparent resistivity; (ii) having reciprocal error $>5\%$; (iii) having contact resistance $>2000\ \Omega$; and (iv) having positive/negative pulse amplitude ratios <0.75 or >1.33 (a measure of waveform symmetry). Of the 2580 reciprocal pairs of measurements, typically 88% remained after filtering. Three-dimensional ERT inversion of the data yields resistivity images that clearly show the main geological formations and geomorphological features. The WMF and RMF exhibit resistivities $<30\ \Omega$ m due to their high clay content, while the SSF exhibits higher resistivities ($>30\ \Omega$ m). This enables the sliding surface, which is postulated to be the interface between SSF and WMF, to be observed in the images [*Wilkinson et al*., 2010; *Chambers et al*., 2011; *Gunn et al*., 2013; *Uhlemann et al*., 2015a].

In *Wilkinson et al*. [2010] a subset of the dipole-dipole data (with $a = 4.75$ m and $n = 2$–4) was used to invert for electrode movements along one of the linear arrays (i.e., in the y direction only). The $n = 1$ data were found to have small but significant sensitivity to movements in the perpendicular direction (i.e., along x) and so were excluded. Here we include the $n = 1$ data since they provide sufficient sensitivity to resolve movements in both directions [*Wilkinson et al*., 2015] (see also Table S1 in the supporting information).

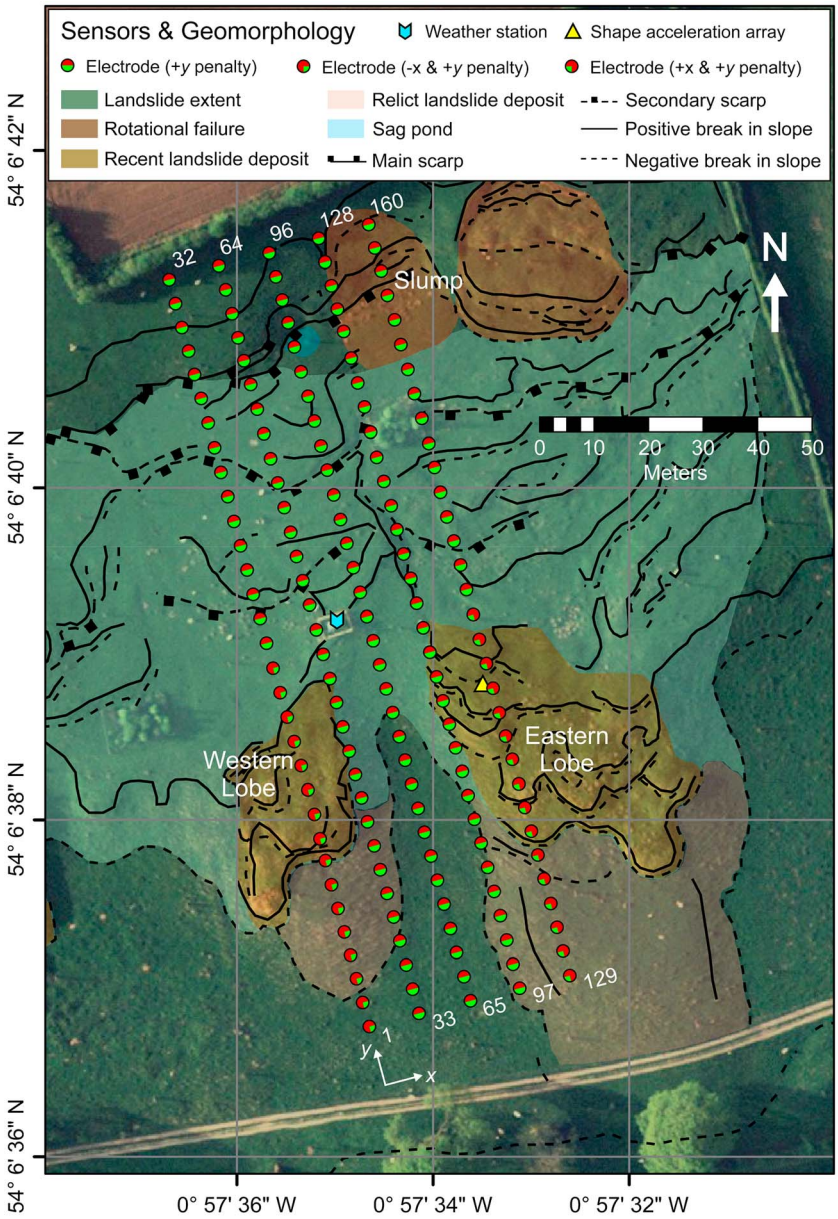


Figure 1. Geomorphological map of the research site indicating different landslide bodies and features. Also shown are the locations of monitoring equipment and electrodes, with identification numbers, and constraint directions (indicated by red circle sectors) shown relative to local site coordinate axes. Aerial photograph © UKP/Getmapping License No. UKP2006/01.

3. Method

In previous studies of displacement inversion using 2-D field data [*Wilkinson et al.*, 2010] and 3-D laboratory tank data [*Wilkinson et al.*, 2015], we found that ratios of ERT data after and before electrode movement could be modeled successfully by a simple approximate forward response model based on a homogeneous subsurface. To regularize the inversion, for each electrode we applied constraints on the magnitude of its displacement and on the displacement component in the local uphill direction [*Wilkinson et al.*, 2015]. Here we modified this approach slightly to allow the uphill constraint to have different strengths in the x and y directions. This was necessary to balance the different sensitivities to displacements in these directions caused by the rectangular geometry of the electrode grid. We now minimize the following objective function

$$\sum_{i=1}^{N}(d_i - f_i)^2 + \alpha\sum_{j=1}^{M}\left\|\boldsymbol{\delta}_j\right\| + \beta\sum_{j=1}^{M}H\left(u_{jy}\delta_{jy}\right)\left|\delta_{jy}\right| + \gamma\sum_{j=1}^{M}H\left(u_{jx}\delta_{jx}\right)\left|\delta_{jx}\right|, \quad (1)$$

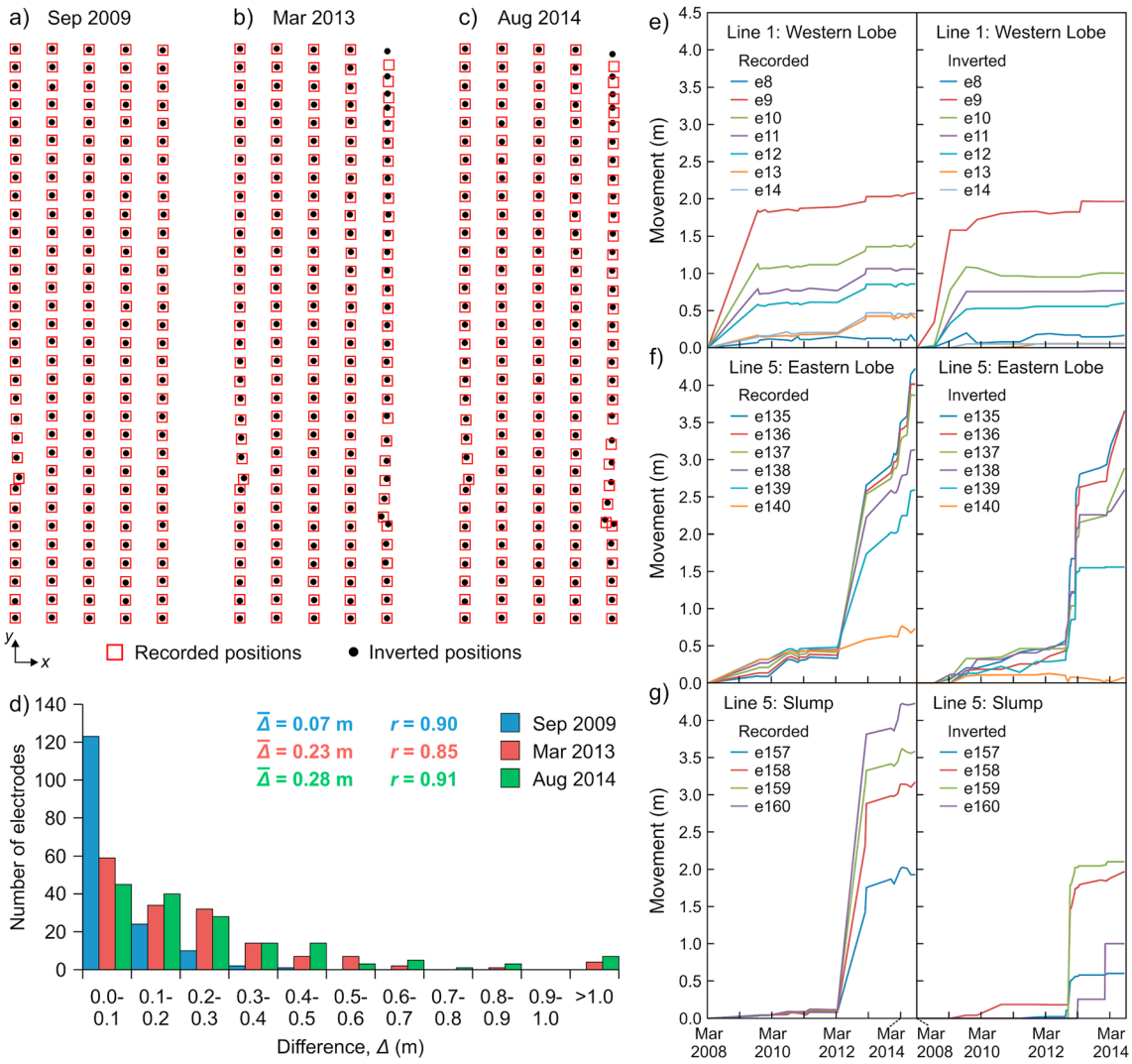


Figure 2. (a–c) Comparisons of recorded (GPS) and inverted positions at indicated times during the monitoring period. (d) Histograms of differences between inverted and recorded positions. (e–g) Comparisons of recorded and inverted movements as a function of time for electrodes in active regions of the landslide.

where there are N measured data and M electrode displacement vectors. The entries of the data vector **d** are the ratios of the present to the baseline measured transfer resistances. The model vector **m** comprises $\boldsymbol{\delta}_j = (\delta_{jx}, \delta_{jy})$, the displacement vectors between the positions at the present and previous time steps, and $r_{1\rightarrow 4}$, which are scalar ratios used to account for bulk changes in the resistivity of the subsurface at the pseudodepths for dipole-dipole levels $n = 1 \rightarrow 4$ [*Wilkinson et al.*, 2010], i.e.,

$$\begin{aligned} m_j &= \delta_{jx} \\ m_{M+j} &= \delta_{jy} \\ m_{2M+n} &= r_n. \end{aligned} \tag{2}$$

The model response vector **f** has entries

$$f_i = r(i)\frac{K_i}{K_i'}, \tag{3}$$

where K_i and K_i' are the initial and current geometric factors of the ith configuration and $r(i)$ is the bulk resistivity ratio for its given n level (i.e., each $r(i) \in \{r_n\}$). Due to the presence of surface topography, calculations of the displacements $\{\boldsymbol{\delta}\}$ and geometric factors $\{K\}$ and $\{K'\}$ necessarily involve further approximations. They are calculated by projecting the electrode positions onto a plane that was least squares fitted to the known

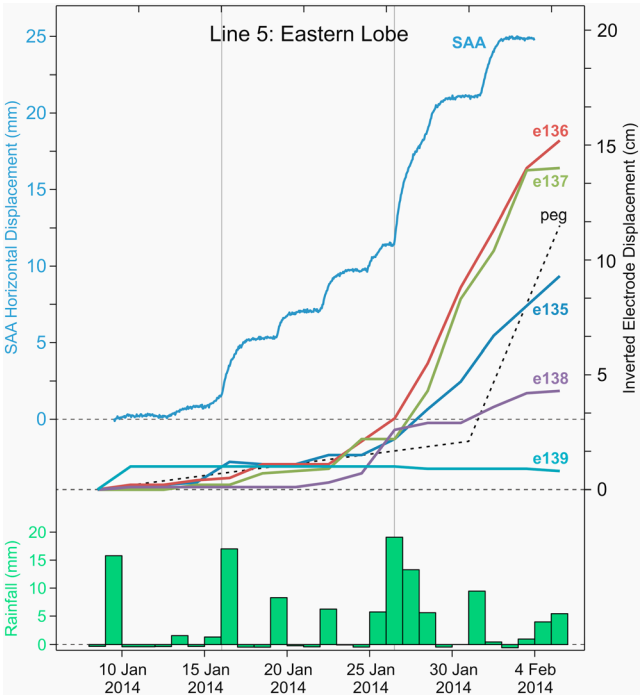


Figure 3. Comparison of SAA movements, inverted electrode movements, estimated marker peg movements, and daily rainfall during a period of landslide activation between January and February 2014.

surface topography for the baseline data. It is these planar projections of displacements and overall positions that are shown in Figures 2 and 3 and compared with GPS and SAA data. But to use the estimated electrode positions in a resistivity inversion, the planar positions are projected back to the baseline topographic surface to give an estimate of the true surface positions (Figure S2). We used similar methods successfully in *Wilkinson et al.* [2010] for movements on a 2-D linear electrode array with topography.

The model constraints are determined by α, the weight of an L^1 constraint on the magnitudes of the displacements, and β and γ, the weights of L^1 constraints on uphill components of the displacements in the x and y directions, respectively. The uphill penalties for electrode j are controlled by u_{jx} and u_{jy}, each of which takes values from {-1, 0, 1} depending on whether displacements are penalized along the negative axis, not penalized, or along the positive axis, respectively. The penalized directions are shown by red segments in Figure 1; there is no uphill penalty for movement toward the green segments (this behavior is ensured by H, the Heaviside step function).

Equation (1) is minimized to find the best fitting $\{\boldsymbol{\delta}\}$ and $\{r_n\}$ using an iterative Gauss-Newton method, at each step solving

$$\left(\mathbf{G}^{\mathrm{T}}\mathbf{G}+\mathbf{A}+\mathbf{B}\right)\Delta\mathbf{m}=\mathbf{G}^{\mathrm{T}}(\mathbf{d}-\mathbf{f})-(\mathbf{A}+\mathbf{B})\,\mathbf{m} \tag{4}$$

to find an update for $\mathbf{m}$, $\Delta\mathbf{m}$, that reduces equation (1). $\mathbf{G}$ is the Jacobian matrix of sensitivities with elements given by

$$\begin{aligned} G_{i,j} &= \frac{\partial f_i}{\partial \delta_{jx}} \\ G_{i,M+j} &= \frac{\partial f_i}{\partial \delta_{jy}} \\ G_{i,2M+n} &= \frac{\partial f_i}{\partial r_n}, \end{aligned} \tag{5}$$

which are calculated numerically by perturbation. The L^1 constraints are implemented by iteratively reweighting the least squares solution procedure [*Farquharson*, 2008]. The reweighting matrices for the displacement magnitude, $\mathbf{A}$, and uphill constraints, $\mathbf{B}$, are diagonal with elements given by

$$\begin{aligned} A_{j,j} &= \alpha\left\|\boldsymbol{\delta}_j\right\|^{-1} \\ A_{M+j,M+j} &= \alpha\left\|\boldsymbol{\delta}_j\right\|^{-1} \\ A_{2M+n,2M+n} &= 0 \end{aligned} \tag{6}$$

and

$$\begin{aligned} B_{j,j} &= \gamma H\left(u_{jx}\delta_{jx}\right)\delta_{jx}{}^{-1} \\ B_{M+j,M+j} &= \beta H\left(u_{jy}\delta_{jy}\right)\delta_{jy}{}^{-1} \\ B_{2M+n,2M+n} &= 0. \end{aligned} \tag{7}$$

Convergence of the solution is enhanced by using a line search to find the minimum along the descent direction at each step. We found that 15 iterations were sufficient to achieve convergence for all the steps in the following examples.

4. Monitoring Movement—Long Term

We reconstructed electrode movements from two sets of data per year, acquired at approximately equal intervals between March 2008 and August 2014. The inversions used the positions acquired from the previous inversion as the starting model for the subsequent step and constraint weights of $\alpha = 0.025\ m^{-1}$, $\beta = 0.025\ m^{-1}$, and $\gamma = 0.050\ m^{-1}$ were applied. The quality of the results did not depend critically on the magnitude of the constraints [*Wilkinson et al*., 2010], but it was found that a stronger uphill constraint was needed in the *x* direction to compensate for the lower sensitivity to movement in this direction. At two stages, over the winters of 2012/2013 and 2013/2014, sequences of extra data taken at much shorter intervals were included to test the ability of the inversion to resolve smaller movements (these are incorporated in this series, but will be examined in detail later).

Figures 2a–2c show the recorded and inverted positions at 3 times after significant periods of movement: (a) after winter 2008/2009 (activity mainly in the western lobe); (b) after winter 2012/2013 (activity mainly in the eastern lobe and slump); and (c) after a more prolonged period of movement beginning in winter 2013/2014 (activity mainly in the eastern lobe). Qualitatively, in terms of location, direction, and magnitude, the inverted movement patterns generally match the recorded displacements well. Figure 2d shows the distribution of differences, Δ, average differences, $\overline{\Delta}$, and uncentered correlation coefficients, *r*, between the measured and inverted movements. The differences tend to increase with time, with average differences increasing from 7 cm to 28 cm over the course of 6 years of monitoring. It should be noted that as in *Wilkinson et al*. [2010, 2015], this is small compared to the along-line electrode spacing (between 1% and 6%). For comparison, the typical repeatability of GPS measurements on the site was ~6 cm. The increase of the differences over time is due to the inversion being damped and hence tending to underestimate the amount of movement. It tends to be skewed toward greater differences in regions with low data density, often near the array corners, such as the slump below the main scarp. Nevertheless, the measured and inverted movements correlate very strongly in all cases ($r \geq 0.85$).

The graphs in Figures 2e–2g compare the recorded and inverted movements of electrodes in the active regions of the landslide over the whole monitoring period, and again, qualitatively, there is very good agreement between observed and inverted periods of activity (note that the observed movements are not evenly distributed in time). Where the inversion fails to recover the movements of a particular electrode, it is typically due to its contributions in equation (1) being dominated by the constraints rather than the data discrepancy. This arises from a combination of small movements and/or few measurements, the latter being due to poor data quality or the location within the electrode grid. For example, electrodes 13 and 14 on the western lobe experienced a modest amount of movement during monitoring but also exhibited poor data quality causing much of their data to be filtered out in the 2013 and 2014 sets (this was especially so for electrode 14). The effect is more pronounced in the slump area, where the inverted movements are considerably smaller than measured. Since these electrodes are at the end of the line, there are fewer data available than for electrodes in the middle. Also, electrode 160 exhibited poor data quality for much of the monitoring period, only occasionally producing usable measurements, so despite it moving by over 4 m, the inversion only recovered a movement of ~1 m.

5. Monitoring Movement—Short Term

The data discrepancy has two contributions; one arising from the difference between the modeled and the real electrode positions and the remainder from effects that are not simulated in the forward model. In addition to random noise and time-varying data quality, the effects of topography and changes in subsurface resistivity are only crudely approximated in the present model. When inverting data with longer time steps, the magnitude of the constraints has to be larger to damp out artifacts that would be caused by the model trying to fit the effects of greater, seasonal changes in the subsurface resistivity.

Two sequences of data at shorter intervals are included in the long-term monitoring period described above. Here the results during one sequence, the landslide activation in the winter of 2014, are examined in detail.

The higher-frequency data were measured on alternate days from 8 January 2014 to 5 February 2014. Since the data were consistently measured at the same time of day, the effects of changing resistivities and varying data quality were not expected to be as great on these short timescales as for the long-term seasonal data sets gathered at 6-monthly intervals. Therefore, the constraints were relaxed to $\alpha = 0.005\,\mathrm{m}^{-1}$, $\beta = 0.005\,\mathrm{m}^{-1}$, and $\gamma = 0.010\,\mathrm{m}^{-1}$. The main activity on the landslide in this period was concentrated on the eastern lobe, in which a borehole SAA had been installed (see Figure 1) to log movement with submillimetric accuracy at hourly intervals. *Smith et al.* [2014] and *Uhlemann et al.* [2015b] showed that movements recorded by the SAA correlated very closely the occurrence of heavier rainfall. The SAA movements at the failure surface depth (~1.5 m) are shown in Figure 3 along with the daily rainfall recorded at the site weather station (Figure 1). The movement rate was initially low (~0.5 mm/d until 15 January), rising to ~1.0 mm/d between 16 and 26 January, before rising again to ~1.5 mm/d between 26 January and 2 February. Each sharp increase in movement rate coincided with the onset of heavier rainfall (indicated by grey vertical lines). The measured SAA movements would have been too small to be detected by GPS or position inversion for the nearest electrode (141). But the inverted movements of electrodes ~10–30 m farther down the slope, in a region of considerably greater instability, exhibited a similar temporal pattern of behavior (electrodes 135–139, see Figure 3), albeit with an order-of-magnitude larger movements. Initially slow movement accelerated between 16 and 26 January and again between 26 January and 5 February. The magnitudes of the movements were also consistent with those estimated from GPS measurements of the positions of surface marker pegs, which were undertaken every 1–2 months. The nearest of the pegs is located between electrodes 135 and 136 and its displacement between 8 January and 5 February was ~12 cm (estimated by linear interpolation and shown by a dashed black line).

6. Discussion

This study is a proof-of-principle demonstration conducted with existing data; consequently, some limitations were present which we discuss here along with aspects for future research. Due to the geometry of the electrode array, the primary dipole-dipole data were collected on separate electrode lines in the *y* direction. Despite this, the inversion couples the movement on all lines together via the global regularization terms in equation (1). Should it be desirable to do so, similar but not identical results could probably be obtained by separate inversions of data on individual lines. Other types of data were measured including equatorial dipole-dipole with current and potential dipoles spanning adjacent lines, and cross-line dipole-dipoles in the *x* direction, but neither type was measured for the entire monitoring period. In our tank experiments [*Wilkinson et al.*, 2015] we found that both equatorial and cross-line dipole-dipoles were useful in inverting movement on a grid array, both for homogeneous and heterogeneous resistivity backgrounds. However, those experiments did not simulate changing resistivity distributions. In tests we found that our inverse method is prone to fitting spurious movements when equatorial dipole-dipole data changes are caused by subsurface resistivity variations, even when the constraints are increased. But cross-line dipole-dipole data could be incorporated (although with five lines, only $n = 1$–2 could be measured). These data were collected from February 2013 onward. Consequently, we reinverted the detailed movement sequence from winter 2014 with this data included, starting from the recorded electrode positions in February 2013. We obtained very similar displacements and temporal behavior as in Figure 3 (the results are shown in Figure S1), suggesting that these data were consistent with the inline dipole-dipole data. The inverted displacements were generally slightly greater with the cross-line data, suggesting that the resolution along the *x* axis was improved (i.e., the influence of the data relative to the damping constraints was increased by incorporating the cross line measurements). Until the relative effects of resistivity changes on equatorial configurations are better understood, when using our method we would recommend that inline and cross-line dipole-dipole data be measured if possible. Of other types of linear ERT measurements, Wenner-Schlumberger are generally less sensitive to electrode displacements, and multiple-gradient typically have intermediate sensitivities (see supporting information). But if multiple data types are available, it might be possible to use one to assess movement and another to invert for resistivity. Dipole-dipole (good displacement resolution) and multiple-gradient (good resistivity resolution) could be a useful combination.

An important topic of future research will be the distinguishability of electrode movements and resistivity changes in various measurement configurations. In 2-D medical imaging it has been shown that provided deformations of the imaging region are nonconformal, the effects of electrode movement can be distinguished from those of isotropic resistivity changes [*Boyle et al.*, 2012]. It is not clear how these results

translate to 3-D ERT when measurements are not available over the whole imaging boundary. But since conformal deformations (e.g., bulk translation or rotation of the grid) do not affect the data, it is almost certainly necessary for some electrodes to be located on stable ground for electrode movement inversion to work.

Other areas for investigation are the types of spatial and temporal constraints used to regularize the inversion. In this study, we modified the approach of *Wilkinson et al*. [2015] to apply the damping to displacements from the last recorded position, rather than the baseline. This enabled the recovery of smaller movements, and since greater movements attract a larger penalty, it seems likely that a sequence of several inversions at intervals short enough to capture the progression of movement would provide greater accuracy than a single inversion of data from the beginning and end of the sequence, but we have yet to demonstrate this explicitly. But we note that even with relatively large time steps over a period of nearly 6.5 years, an average accuracy of 6% of the electrode spacing was achieved. In previous studies [*Wilkinson et al*., 2010, 2015] we found that using displacement inversion significantly reduced ERT imaging artifacts caused by incorrect electrode positions. Here by using the inverted rather than the original 2008 positions in a resistivity inversion of the August 2014 data, we found that the average resistivity model error was reduced from 35% to 11% (see Figure S2), which is consistent with the average accuracy of the inverted positions [*Zhou and Dahlin*, 2003].

Other possibilities to regularize the inversion could include spatial smoothness constraints, constraining the displacements against a reference model provided by an interpolation of sparsely distributed marker peg positions [*Uhlemann et al*., 2015a], or if reconstructing past movement sequences, inverting for movement between recorded GPS positions before and after the ERT data acquisition time (this last possibility would remove the requirement for topographic constraints).

7. Conclusions

With research and applications of 4-D ERT for natural and artificial unstable slopes becoming more prevalent, both as tools for fundamental understanding of hydraulically driven failure processes and as early warning systems in safety-critical infrastructure, it is vital that methods are developed to determine the electrode positions. Without sufficiently accurate knowledge of electrode movements at timescales commensurate with landslide activity, the quantitative capabilities of geoelectrical monitoring will be severely curtailed. In this letter, we described a novel inversion technique for geoelectrical data that is capable of tracking the movements of electrodes over timescales of days to years. The results demonstrate, for the first time using data from a field installation on a natural unstable slope, that position inversion can recover movements along *both* surface directions on a grid of ERT electrodes. The positions were recovered with typical accuracies of $<$10% of the electrode spacing, which is very similar to that achieved at the same test site using interpolation of GPS measurements of a sparse set of marker pegs [*Uhlemann et al*., 2015a]. But position inversion achieves this at higher temporal frequency without the need for manual site visits. Of particular interest is the ability of this method to detect much shorter displacements, of the order of 1% of the electrode spacing, if other changes in the data unrelated to movement (e.g., subsurface resistivity variations) are small. This suggests that joint resistivity and position inversion algorithms, which are under active development [*Loke et al*., 2015], might reliably detect motion at these scales regardless of geoelectrical changes occurring below the surface. Then continuous monitoring with future ERT-based early warning systems could provide robust indications of surface motion as well as the hydrogeophysical state of the ground beneath. Although currently in its nascent stages, we envisage that electrode movement inversion could be routinely applied to geoelectrical monitoring of unstable ground in many situations beyond slope stability, including karst terrain, shrink-swell potential, and volcanic deformation.

Acknowledgments

We would like to convey our sincerest gratitude to the Gibsons (the landowners) for their involvement and cooperation throughout this research and the Editor and reviewers for their helpful comments. P.W., J.C., S.U., and P.M. were supported by the Natural Environment Research Council (NERC). A.S. and N.D. were supported by the Engineering and Physical Sciences Research Council. This paper is published with the permission of the Executive Director of the BGS (NERC). The data used in this paper are archived by BGS and are available from the authors in accordance with RCUK Concordat on Open Research Data.

References

Abdoun, T., V. Bennett, T. Desrosiers, J. Simm, and M. Barendse (2012), Asset management and safety assessment of levees and earthen dams through comprehensive real-time field monitoring, *Geotech. Geol. Eng.*, *31*(3), 833–843.

Aryal, A., B. A. Brooks, and M. E. Reid (2015), Landslide subsurface slip geometry inferred from 3–D surface displacement fields, *Geophys. Res. Lett.*, *42*, 1411–1417, doi:10.1002/2014GL062688.

Bièvre, G., D. Jongmans, T. Winiarski, and V. Zumbom (2012), Application of geophysical measurements for assessing the role of fissures in water infiltration within a clay landslide (Trièves area, French Alps), *Hydrol. Process.*, *26*, 2128–2142.

Bogaard, T. A., and R. Greco (2015), Landslide hydrology: From hydrology to pore pressure, *WIREs Water*, doi:10.1002/wat2.1126.

Booth, A. M., M. P. Lamb, J.-P. Avouac, and C. Delacourt (2013), Landslide velocity, thickness, and rheology from remote sensing: La Clapière landslide, France, *Geophys. Res. Lett.*, *40*, 4299–4304, doi:10.1002/grl.50828.

Boyle, A., A. Adler, and W. R. B. Lionheart (2012), Shape deformation in two-dimensional electrical impedance tomography, *IEEE Trans. Med. Imaging*, *31*, 2185–2193.

Boyle, A., P. B. Wilkinson, J. E. Chambers, N. Lesparre, and A. Adler (2014), Slope stability monitoring through impedance imaging, in *Proceedings of 15th International Conference on Electrical Impedance Tomography*, p. 42, IOP, Ontario, Canada.

Chambers, J. E., P. B. Wilkinson, O. Kuras, J. R. Ford, D. A. Gunn, P. I. Meldrum, C. V. L. Pennington, A. L. Weller, P. R. N. Hobbs, and R. D. Ogilvy (2011), Three-dimensional geophysical anatomy of an active landslide in Lias Group mudrocks, Cleveland Basin, UK, *Geomorphology*, *125*, 472–484.

Chambers, J. E., D. A. Gunn, P. B. Wilkinson, P. I. Meldrum, E. Haslam, S. Holyoake, M. Kirkham, O. Kuras, A. Merritt, and J. Wragg (2014), 4D electrical resistivity tomography monitoring of soil moisture dynamics in an operational railway embankment, *Near Surf. Geophys.*, *12*, 61–72.

Dijkstra, T., N. Dixon, C. Crosby, M. Frost, D. Gunn, P. Fleming, and J. Wilks (2014), Forecasting infrastructure resilience to climate change, *Proc. Inst. Civ. Eng.*, *167*, 269–280.

Dixon, N., M. P. Spriggs, A. Smith, P. Meldrum, and E. Haslam (2015), Quantification of reactivated landslide behaviour using acoustic emission monitoring, *Landslides*, *12*, 549–560.

Farquharson, C. G. (2008), Constructing piecewise-constant models in multidimensional minimum-structure inversions, *Geophysics*, *73*, K1–K9.

Giannakis, I., P. Tsourlos, N. Papadopoulos, and A. Giannopoulos (2012), A method to detect displacements of borehole electrodes through electrical resistivity tomography, in *Proceedings of 18th European Meeting of Environmental and Engineering Geophysics*, CO3, EAGE Publ., Paris, France.

Gunn, D. A., J. E. Chambers, P. R. N. Hobbs, J. R. Ford, P. B. Wilkinson, G. O. Jenkins, and A. Merritt (2013), Rapid observations to guide the design of systems for long-term monitoring of a complex landslide in the Upper Lias clays of North Yorkshire, UK, *Quart. J. Eng. Geol. Hydrogeol.*, *46*, 323–336.

Gunn, D. A., et al. (2014), Moisture monitoring in clay embankments using electrical resistivity tomography, *Constr. Build. Mater.*, doi:10.1016/j.conbuildmat.2014.06.007.

Hibert, C., G. Ekström, and C. P. Stark (2014), Dynamics of the Bingham Canyon Mine landslides from seismic signal analysis, *Geophys. Res. Lett.*, *41*, 4535–4541, doi:10.1002/2014GL060592.

Kim, J.-H., M.-J. Yi, R. Supper, and D. Ottowitz (2014), Simultaneous inversion of resistivity structure and electrode locations in ERT, in *Proceedings of 20th European Meeting of Environmental and Engineering Geophysics*, WeOlym10, EAGE Publ., Athens, Greece.

LaBrecque, D. J., M. Miletto, W. Daily, A. Ramirex, and E. Owen (1996), The effects of noise on Occam's inversion of resistivity tomography data, *Geophysics*, *61*, 538–548.

Lebourg, T., M. Hernandez, S. Zerathe, S. El Bedoui, H. Jomard, and B. Fresia (2010), Landslides triggered factors analysed by time lapse electrical survey and multidimensional statistical approach, *Eng. Geol.*, *114*, 238–250.

Lehmann, P., and D. Or (2012), Hydromechanical triggering of landslides: From progressive local failures to mass release, *Water Resour. Res.*, *48*, W03535, doi:10.1029/2011WR010947.

Loke, M. H., P. B. Wilkinson, and J. E. Chambers (2015), Rapid inversion of data from 2-D and from 3-D resistivity surveys with shifted electrodes, in *Proceedings of 21st European Meeting of Environmental and Engineering Geophysics*, We21B11, EAGE Publ., Turin, Italy.

Merritt, A. J., J. E. Chambers, W. Murphy, P. B. Wilkinson, L. J. West, D. Gunn, P. I. Meldrum, M. Kirkham, and N. Dixon (2014), 3D ground model development for an active landslide in Lias mudrocks using geophysical, remote sensing and geotechnical methods, *Landslides*, *11*, 537–550.

Niesner, E. (2010), Subsurface resistivity changes and triggering influences detected by continuous geoelectrical monitoring, *Leading Edge*, *29*, 952–955.

Oldenborger, G. A., P. S. Routh, and M. D. Knoll (2005), Sensitivity of electrical resistivity tomography data to electrode position errors, *Geophys. J. Int.*, *163*, 1–9.

Perrone, A., V. Lapenna, and S. Piscitelli (2014), Electrical resistivity tomography technique for landslide investigation: A review, *Earth Sci. Rev.*, *135*, 65–82.

Sjodahl, P., T. Dahlin, and S. Johansson (2009), Embankment dam seepage evaluation from resistivity monitoring data, *Near Surf. Geophys.*, *7*, 463–474.

Sjodahl, P., T. Dahlin, and S. Johansson (2010), Using the resistivity method for leakage detection in a blind test at the Rossvatn embankment dam test facility in Norway, *Bull. Eng. Geol. Environ.*, *69*, 643–658.

Smith, A., N. Dixon, P. Meldrum, E. Haslam, and J. Chambers (2014), Acoustic emission monitoring of a soil slope: Comparisons with continuous deformation measurements, *Géotech. Lett.*, *4*, 255–261.

Supper, R., D. Ottowitz, B. Jochum, J.-H. Kim, A. Römer, I. Baron, S. Pfeiler, M. Lovisolo, S. Gruber, and F. Vecchiotti (2014), Geoelectrical monitoring: An innovative method to supplement landslide surveillance and early warning, *Near Surf. Geophys.*, *12*, 133–150.

Uhlemann, S., P. B. Wilkinson, J. E. Chambers, H. Maurer, A. J. Merritt, D. A. Gunn, and P. I. Meldrum (2015a), Interpolation of landslide movements to improve the accuracy of 4D geoelectrical monitoring, *J. Appl. Geophys.*, *121*, 93–105.

Uhlemann, S., A. Smith, J. E. Chambers, N. Dixon, T. Dijkstra, E. Haslam, P. I. Meldrum, A. J. Merritt, D. A. Gunn, and J. Mackay (2015b), Assessment of ground-based monitoring techniques applied to landslide investigations, *Geomorphology*, *253*, 438–451.

Wilkinson, P. B., J. E. Chambers, M. Lelliott, G. P. Wealthall, and R. D. Ogilvy (2008), Extreme sensitivity of crosshole electrical resistivity tomography measurements to geometric errors, *Geophys. J. Int.*, *173*, 49–62.

Wilkinson, P. B., J. E. Chambers, P. I. Meldrum, D. Gunn, R. D. Ogilvy, and O. Kuras (2010), Predicting the movements of permanently installed electrodes on an active landslide using time-lapse geoelectrical resistivity data only, *Geophys. J. Int.*, *183*, 543–556.

Wilkinson, P. B., S. Uhlemann, J. E. Chambers, P. I. Meldrum, and M. H. Loke (2015), Development and testing of displacement inversion to track electrode movements on 3-D electrical resistivity tomography monitoring grids, *Geophys. J. Int.*, *200*, 1566–1581.

Yamada, M., H. Kumagai, Y. Matsushi, and T. Matsuzawa (2013), Dynamic landslide processes revealed by broadband seismic records, *Geophys. Res. Lett.*, *40*, 2998–3002, doi:10.1002/grl.50437.

Zhou, B., and T. Dahlin (2003), Properties and effects of measurement errors on 2D resistivity imaging surveying, *Near Surf. Geophys.*, *1*, 105–117.